The Astrophysical Journal, 594:1033–1048, 2003 Sepember 10


# THE MAGNETIC HELICITY BUDGET OF SOLAR ACTIVE REGIONS AND CORONAL MASS EJECTIONS

A. Nindos
Section of Astrogeophysics, Department of Physics, University of Ioannina, Ioannina GR-45110, Greece; anindos@cc.uoi.gr

J. Zhang
Center for Earth Observing and Space Research, George Mason University, Fairfax, VA 22030

and

H. Zhang
National Astronomical Observatories, Chinese Academy of Sciences, A20 Datun Road, Chaoyang, Beijing 100012, People's Republic of China

*Received 2003 February 17; accepted 2003 May 23*

## ABSTRACT

We compute the magnetic helicity injected by transient photospheric horizontal flows in six solar active regions associated with halo coronal mass ejections (CMEs) that produced major geomagnetic storms and magnetic clouds (MCs) at 1 AU. The velocities are computed using the local correlation tracking (LCT) method. Our computations cover time intervals of 110–150 hr, and in four active regions the accumulated helicities due to transient flows are factors of 8–12 larger than the accumulated helicities due to differential rotation. As was first pointed out by Démoulin and Berger, we suggest that the helicity computed with the LCT method yields not only the helicity injected from shearing motions but also the helicity coming from flux emergence. We compare the computed helicities injected into the corona with the helicities carried away by the CMEs using the MC helicity computations as proxies to the CME helicities. If we assume that the length of the MC flux tubes is $l = 2$ AU, then the total helicities injected into the corona are a factor of 2.9–4 lower than the total CME helicities. If we use the values of $l$ determined by the condition for the initiation of the kink instability in the coronal flux rope or $l = 0.5$ AU then the total CME helicities and the total helicities injected into the corona are broadly consistent. Our study, at least partially, clears up some of the discrepancies in the helicity budget of active regions because the discrepancies appearing in our paper are much smaller than the ones reported in previous studies. However, they point out the uncertainties in the MC/CME helicity calculations and also the limitations of the LCT method, which underestimates the computed helicities.

*Subject heading:* solar-terrestrial relations — Sun: activity — Sun: corona — Sun: coronal mass ejections (CMEs) — Sun: magnetic fields — Sun: photosphere

## 1. INTRODUCTION

Coronal mass ejections (CMEs) are spectacular large-scale expulsions of mass, magnetic flux, and magnetic helicity from the lower corona into the interplanetary medium. They are also the primary cause of the largest and most damaging space weather disturbances (Gosling 1993). CMEs are observed with a coronagraph above the occulting disk as projections on the plane of the sky, and consequently their correlation with the configuration and evolution of the underlying solar structures is not straightforward. Nevertheless soft X-ray observations obtained with the Soft X-Ray Telescope (SXT) on board the *Yohkoh* satellite and EUV observations with the EUV Imaging Telescope (EIT) on board the *Solar and Heliospheric Observatory* (*SOHO*) have greatly eased the tasks of identifying CME counterparts near the solar surface and of following the early development of the eruptions. The low corona CME counterparts (see the article by Hudson & Cliver 2001, for a detailed review) may include coronal waves discovered by EIT (EIT waves; see Thompson et al. 1998), EUV and/or soft X-ray "dimmings" (Rust 1983; Sterling & Hudson 1997), and long-duration soft X-ray events that occur after the CME eruption (e.g., Sheeley et al. 1975). Furthermore, SXT data reveal a relationship between coronal X-ray sigmoids (Rust & Kumar 1996) and eruptivity (Canfield, Hudson, & McKenzie 1999). A flare may also destabilize an adjacent transequatorial loop structure, thus launching a CME (Khan & Hudson 2000). We note that not every CME is accompanied by all the noncoronagraphic signatures listed here.

The most generally accepted explanation for the cause of CMEs is that they are produced by a loss of stability or equilibrium of the coronal magnetic field. Several models for the initiation of CMEs have been developed (see the reviews by Klimchuk 2000; Forbes 2000). In some of them (e.g., Mikić & Linker 1994) destabilization of coronal arcades occurs when magnetic shear exceeds a critical threshold. Reconnection occurring in a current sheet within the arcade could then produce not only newly closed arcades but also a twisted flux rope that is expelled from the corona. Other models advocate the existence of twisted magnetic flux ropes in the corona before the ejection. Then slow converging motions of two photospheric field sources (Forbes & Priest 1995) or fast injection of new magnetic flux (Chen 1996) may lead to the ejection of the flux rope. All these models imply that the interplanetary magnetic clouds (MCs) that are observed at 1 AU come from ejections of magnetic flux ropes from the solar corona.

All models for CME initiation require information about the photospheric magnetic field evolution (motions and flux emergence/submergence) leading up to eruption. In principle, all patterns of suitable photospheric evolution (i.e., flux emergence, shearing, twisting, and converging

motions) may provide a triggering mechanism to cause the system to become unstable, initiating the launch of a CME. Observations should provide constraints on the range and efficiency of such possible motions or patterns of evolution. In this direction, Feynman & Martin (1995) found a strong correlation between newly emerging magnetic field and filament eruptions, which they took as proxies for CMEs. Lara, Gopalswamy, & DeForest (2000) studied eight eruptive events and found that the total magnetic flux over the active region did not show significant changes. But they found significant changes in the flux over small subregions of the overall active region associated with the CME. They also found that the changes in flux occur over timescales of several hours to days. Subramanian & Dere (2001) report that CMEs linked to active regions are often associated with small-scale emerging or canceling flux over timescales of 6–7 hr.

The magnetic field carried away by the CMEs is twisted. CME activity is considered a valve through which the Sun gets rid of excess magnetic helicity (e.g., van Driel–Gesztelyi et al. 1999). The magnetic helicity is a quantitative measure of the chiral properties of the structures observed in the solar atmosphere (see § 2.2). In a closed volume it is a fairly well-conserved quantity. In an open volume such as the solar atmosphere, however, magnetic helicity can change either because of the emergence of new twisted field lines that cross the photospheric surface (e.g., Leka et al. 1996) and/or by horizontal motions on the photospheric surface. Such motions may come either from differential rotation and/or from transient photospheric shearing flows. Recently Démoulin et al. (2002b), Green et al. (2002), and Nindos & Zhang (2002) found that differential rotation cannot provide the required helicity to the magnetic field ejected to the interplanetary medium by CMEs. Furthermore, Nindos & Zhang (2002) studied a CME-productive active region that was the site of intense transient shearing motions and found that the observed motions cannot account for the helicity removed by the CMEs linked to the active region.

In this paper we study the photospheric magnetic field evolution of six active regions that were the sources of CMEs that caused major geomagnetic storms and produced MCs observed by *Wind* spacecraft. The active regions have been selected from the lists presented by Zhang et al. (2003), who studied the solar sources of all major geomagnetic storms between 1996 and 2000. Using high-cadence Michelson Doppler Imager (MDI) photospheric magnetograms and white-light images we monitor the active regions for several days. Using local correlation tracking techniques we evaluate the contribution of the observed transient photospheric flows to the helicity carried away by the CMEs. For such study, the selected active regions are ideal because the development of MCs associated with CMEs linked to the active regions gives direct information about the CME helicities.

## 2. OBSERVATIONS AND DATA ANALYSIS

### 2.1. *Data*

In Table 1 we present the active region complexes that we studied. These active regions were associated with halo CMEs that produced major geomagnetic storms and also produced MCs observed by *Wind* spacecraft. Identifying the solar source for a given geomagnetic storm and/or MC is not a straightforward process. On the basis of LASCO/EIT data, Zhang et al. (2003) have identified the solar sources of 27 major geomagnetic storms occurring between 1996 and 2000. Their approach to the identification consists of two steps. The first step is to use a fixed 30–120 hr backward time window to select candidate front-side halo CMEs, which are often not unique (front-side halo CMEs are usually apparent in EIT 195 Å images as dimmings, "EIT waves," localized brightenings, or posteruption arcades). The second step is to use solar-wind data to provide further constraints. One of the constraints is to use the solar wind interplanetary CME speed to calculate an adaptive time window, which is based on the assumption that an initially fast solar CME would decrease its velocity in the transit from the Sun to the Earth. From the lists of Zhang et al. (2003) of the solar sources of major geomagnetic storms we selected six active region complexes that (1) were associated with at least one solar CME that produced a MC and (2) for which high-cadence MDI data were available for at least half the time interval they needed to cross the disk from heliographic longitude $-50^\circ$ to heliographic longitude $50^\circ$.

Using 1 minute cadence MDI longitudinal magnetic field data we studied the evolution of the observed horizontal flow patterns in the active regions for the time intervals listed in Table 1. In Table 1 we also give the corresponding locations on the solar disk of the central part of each active region complex. We also present the mean absolute value of the magnetic flux of the active regions (average of both polarities). Our 1 minute cadence MDI database consists of both high-resolution (HR) images (with pixel size $0\farcs6$ and field of view $420'' \times 420''$ centered around disk center) and full-disk (FD) images (with pixel size about $2''$). The time intervals when HR images have been used are indicated by the shaded areas in Figures 13, 14, 16, and 17 (no HR images were available for AR 8210 and AR 9182). For the computation of horizontal velocity fields in the umbrae and

TABLE 1
Active Regions

| NOAA Active Region | Start Location | Start Date, Time (UT) | End Location | End Date, Time (UT) | $\lvert\Phi\rvert$[a] ($\times 10^{22}$ Mx) |
|---|---|---|---|---|---|
| 8210 | S17E42 | 1998 Apr 28, 0000 | S17W37 | 1998 May 4, 0120 | 1.6 |
| 8375 | N18E20 | 1998 Nov 3, 0000 | N18W42 | 1998 Nov 7, 1235 | 1.5 |
| 9114, 9115, 9122 | N17E41 | 2000 Aug 5, 2100 | N17W11 | 2000 Aug 10, 2035 | 3.1 |
| 9182 | N00E38 | 2000 Oct 6, 0000 | N02E46 | 2000 Oct 11, 2335 | 1.2 |
| 9201 | N17E35 | 2000 Oct 20, 1800 | N19W34 | 2000 Oct 25, 2320 | 1.9 |
| 9212, 9213, 9218 | N10E45 | 2000 Oct 31, 0000 | N10W40 | 2000 Nov 6, 1020 | 4.0 |

[a] Mean absolute value of the magnetic flux of the active regions (average of both polarities).

penumbrae of sunspots we used 1 minute cadence white-light MDI images when they were available (these time intervals are indicated by the horizontal lines in the top panels of Figures 12, 13, 14, 16, and 17; see also § 6). Both HR and FD white-light images have been used. Their spatial resolution is the same as the spatial resolution of the magnetic field HR and FD images. In our database the HR white-light images are available when HR magnetograms are available.

We also used 96 minute cadence full-disk MDI magnetograms for the study of the overall evolution of the active regions. These data were especially useful for the qualitative study of the evolution of the active regions when high-cadence MDI data were not available. We also used photospheric vector magnetograms of the active regions obtained by the Huairou Solar Observing Station (HSOS) magnetograph (Ai & Hu 1986; Wang, Ai, & Deng 1996). Usually the HSOS data are available every day from about 23:30 to 06:30 UT, with varying cadence and spatial resolution of about 2″. The line-of-sight and transverse components of the magnetic field are measured at the wing and center of the Fe I 5324.19 Å line, respectively. The 180° ambiguity for the transverse field components is resolved with a linear force-free field method to best fit the azimuth (Wang & Abramenko 2000). Finally, we studied the coronal evolution of the active regions using SXT and EIT images that were processed with the standard "solarsoft" software.

### 2.2. *Computation of Magnetic Helicity Change Rate Due to Observed Horizontal Motions*

The relative magnetic helicity (hereafter referred to as helicity) of a field $\boldsymbol{B}$ within the entire coronal volume $V$ with respect to the helicity of a reference field $\boldsymbol{B}_p$ having the same distribution of vertical magnetic flux on the surface $S$ surrounding $V$ is defined as

$$H = \int_V \boldsymbol{A} \cdot \boldsymbol{B}\, dV - \int_V \boldsymbol{A}_p \cdot \boldsymbol{B}_p\, dV \ . \tag{1}$$

Being a potential field it is a convenient choice for $\boldsymbol{B}_p$. The quantity $\boldsymbol{A}_p$ is the corresponding vector potential satisfying $\nabla \cdot \boldsymbol{A}_p = 0$, and it is horizontal on the lower boundary of $S$, which is the photospheric surface $S_p$. Then the term $\int_V \boldsymbol{A}_p \cdot \boldsymbol{B}_p\, dV$ vanishes (Berger 1988). The temporal evolution of helicity across the photospheric boundary $S_p$ can be separated into a tangential term $dH/dt|_t$ and a normal term $dH/dt|_n$. Then according to Berger (1999) we get

$$\left.\frac{dH}{dt}\right|_t = -2 \oint (\boldsymbol{v}_t \cdot \boldsymbol{A}_p) B_n\, dS_p \ , \tag{2}$$

$$\left.\frac{dH}{dt}\right|_n = 2 \oint (\boldsymbol{A}_p \cdot \boldsymbol{B}_t) v_n\, dS_p \ , \tag{3}$$

where $B_t$ and $B_n$ are the tangential and normal components of the magnetic field on the photosphere and $\boldsymbol{v}_t$ and $\boldsymbol{v}_n$ are the tangential and normal components of the photospheric velocity field. Equation (2) gives the change of helicity due to differential rotation and/or transient photospheric shearing and twisting motions while equation (3) gives the change of helicity due to the emergence of twisted field lines that cross the photosphere.

For each active region we compute the rate of helicity changes due to observed horizontal transient motions using 1 minute cadence MDI images. First, for all MDI images we remove solar differential rotation, taking as reference time the time when the active region complex passes through the central meridian. For the FD high-cadence images this rotational mapping is done at new grids with pixel size 1″.

MDI magnetogram data suffer from instrumental effects. Berger & Lites (2003) analyzed simultaneous Advanced Stokes Polarimeter (ASP) and MDI magnetograms and found that MDI underestimates the flux densities in a linear way for MDI pixels below 1200 G by approximately a factor of 1.54. For flux densities higher than 1200 G the underestimation becomes nonlinear and the MDI measurements saturate at about 1300 G, whereas the corresponding ASP fields increase. This underestimation seems to be inherent to the MDI calibration and does not result from the different instrument resolutions (see also Green et al. 2003). This conclusion is verified by the work by Nindos et al. (2002), who compared microwave sunspot images made with the VLA and models of the sunspot radio emission that use MDI data for the magnetic field extrapolations. Therefore we correct all MDI field values by a factor of 1.54. To evaluate the nonlinear behavior of MDI measurements above 1200 G we multiply the fields above 1200 G by a factor of 1.9, which comes from the larger difference between ASP and MDI measurements when MDI values saturate (see Berger & Lites 2003; Green et al. 2003). Consequently the corrected MDI flux $\Phi_{\rm cor}$ should be given by

$$\Phi_{\rm cor} = 1.54(\Phi + 0.23\Phi_{B>1200\,\rm G}) \ . \tag{4}$$

Our nonlinear correction contributes to only a 10%–15% increase after the linear correction has been taken into account. Note also that the corrected MDI measurements are consistent with the corresponding Mount Wilson sunspot magnetic field measurements. We use equation (4) in all the subsequent calculations that involve magnetic fields measured by the MDI.

We compute the rate of helicity change due to the observed horizontal motions (other than differential rotation) by using the method described by Chae et al. (2001). For this calculation the vertical component of the magnetic field is required, which is different from the longitudinal component of the magnetic field when the active region is not at disk center. We assume that the photospheric magnetic field is vertical; therefore the longitudinal field yields the vertical field if we know the heliocentric angle of the active region. We estimate the errors introduced by this assumption by using the HSOS vector magnetograms (see § 6). The value of $\boldsymbol{A}_p$ is computed using the properties of Fourier transforms (see eqs. [4] and [5] in Chae 2001). The velocities $\boldsymbol{v}_{\rm LCT}$ associated with the observed photospheric horizontal motions are computed using the local correlation tracking (LCT) technique (November & Simon 1988). The relation between the computed values of $\boldsymbol{v}_{\rm LCT}$ and $\boldsymbol{v}_t$ that appears in equation (2) is discussed in §§ 6 and 7. Two parameters are critical to the accuracy of LCT: the FWHM $w$ of the apodizing function and the time interval between a pair of images, $\Delta T$. After several tests we choose $w = 7\farcs5$ and $\Delta T = 15$–$20$ minutes. This combination yields the smallest number of velocity vectors measured with maximum cross-correlation smaller than 0.8 and the smallest number of velocity vectors with absolute values higher than 1 km s$^{-1}$ (following Nindos & Zirin 1998, we reject such velocities).

## 3. EVOLUTION OF THE PHOTOSPHERIC MAGNETIC FIELD

### 3.1. *Active Region NOAA 8210*

AR 8210 produced several major flares and CMEs during its disk passage in 1998 late April–early May. Its evolution has been described by Warmuth et al. (2000) while selected events associated with it have been discussed by Thompson et al. (2000), Sterling & Moore (2001), Sterling et al. (2001), Pohjolainen et al. (2001), and Wang et al. (2002). Figure 1 shows that the leading part of the active region is predominantly positive and the trailing part predominantly negative, suggesting that AR 8210 does not follow the Hale-Nicholson polarity rule for cycle 23. When the active region appeared at the east limb, its main sunspot had already developed a $\delta$-configuration; see the white patch north of the main negative-polarity spot in the April 28, 12:51 UT frame of Figure 1. The April 28–30 frames of Figure 1 show the decay of this $\delta$-configuration. This process results partly from cancellation events and partly because the area of positive polarity moves away from the negative flux concentration (see the velocity fields in the corresponding frames of Fig. 2). Simultaneously negative flux emerges south of the main negative penumbra (see Fig. 1) and new bipoles east, southeast, south, and west of the main spot. Meanwhile the main spot has been rotating clockwise and this shows better after about midday of April 30 (see Fig. 2). On May 1 new negative flux emerges east of the main umbra, and a new $\delta$-configuration is formed (Warmuth et al. 2000). Rapid clockwise and counterclockwise flows of the new flux carry much of it away from the main spot along locations close to the sheared neutral line (see the May 1–2 frames in Figs. 1–2). Note that the clockwise flow dominates the motions of the negative-polarity magnetic elements while most of the positive-polarity magnetic elements move counterclockwise. Meanwhile from late May 1 clockwise converging motions of positive flux elements occur north of the main spot while converging, twisting, and shearing motions also occur west and northwest of the main spot.

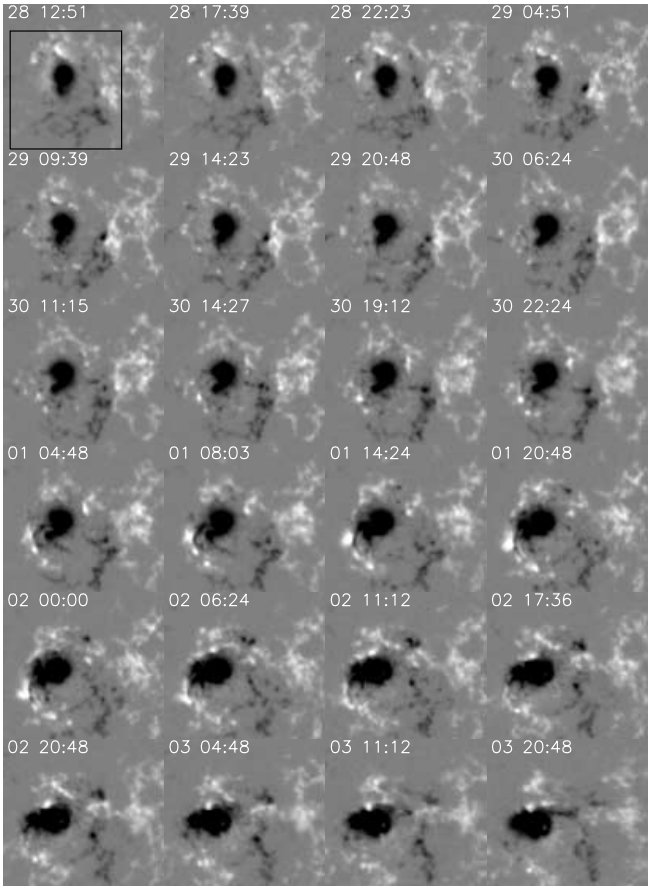


FIG. 1.—Selected MDI images that show the evolution of AR 8210 for the time interval given in Table 1. The black frame marks the area that appears in Fig. 2. In this and subsequent solar images solar north is up and solar west to the right.

### 3.2. *Active Region NOAA 8375*

The proper motions in this active region have been studied by Yurchyshyn & Wang (2001b). In Figure 3 we present selected images from the active region's evolution

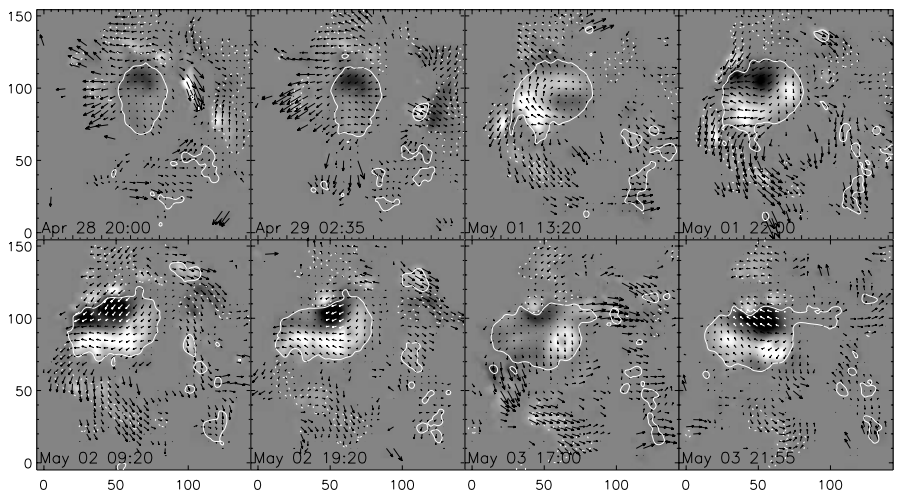


FIG. 2.—Averages over 1 hr of the computed velocity vectors and the corresponding $G = -2\boldsymbol{v}_{\rm LCT} \cdot \boldsymbol{A}_p B_n$ (gray-scale images) for AR 8210. The middle of each time interval is indicated in the panels. The maximum arrow length measures velocity of 0.7 km s$^{-1}$. The full and dotted contours represent longitudinal magnetic field strengths of $-200$ and 200 G, respectively. The axis labels denote arcseconds on the solar photosphere.

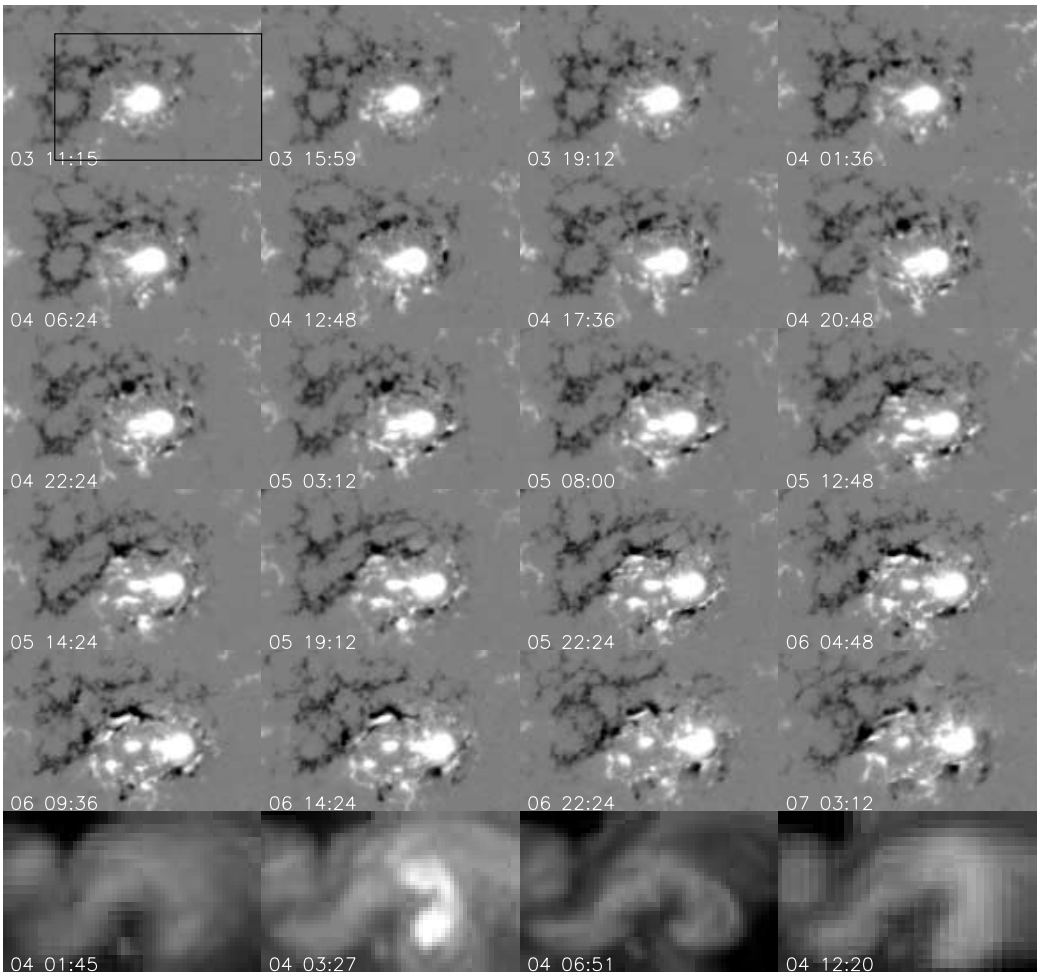


FIG. 3.—Same as Fig. 1 but for AR 8375. The bottom row shows SXT images of the active region. The black frame marks the area that appears in Fig. 4.

while in Figure 4 we show the computed velocities at four characteristic times. In the movies that we made, a radial outflow of moving magnetic features (MMFs; e.g., see Harvey & Harvey 1973) from the sunspot's moat can be seen from November 2. Because of the outflow, already on November 3, 11:15 UT several patches of magnetic elements can be seen around the sunspot. From November 3 the radial outflow is stronger in the northeastern and southeastern directions, and this pattern persists for almost 48 hr (this trend is not so apparent in Fig. 3 but can be seen clearly

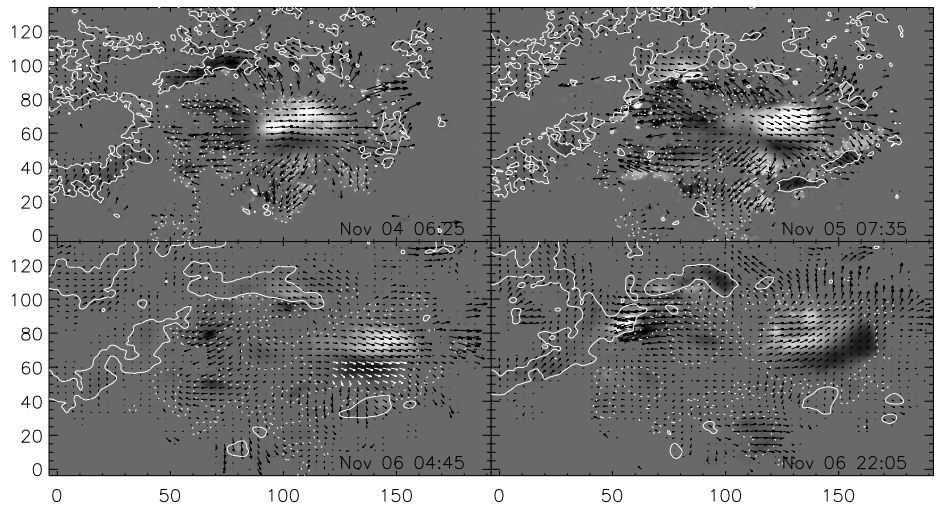


FIG. 4.—Same as Fig. 2 but for AR 8375. The maximum arrow length measures velocity of 0.5 km $s^{-1}$.

in the November 4 and 5 velocity maps presented in Fig. 4). At the same time, from November 3 the whole sunspot starts moving westward. Because of these large-scale flow patterns magnetic elements moving away from the sunspot either cancel opposite-polarity magnetic fields or merge with same-polarity magnetic fields. In Figure 3 such events can be seen all over around the sunspot. Figure 3 gives the impression that after about November 4, 12:48 UT, relatively weak magnetic field structures at the western part of the active region are gradually swept away by the flow associated with the fast-moving sunspot. The eastern outflow from the sunspot decreases after November 5 (see Fig. 4, *bottom left*). Also after November 5–6 the sunspot's westward motion somewhat decreases (see Fig. 4, *bottom right*), and instead of moving westward the sunspot moves northwestward.

AR 8375 was the site of significant flare and CME activity. Selected events that occurred in AR 8375 have been presented by Wang et al. (2000), Yurchyshyn et al. (2000), Yurchyshyn & Wang (2001a), and Zhang & Wang (2001). For a detailed presentation of the coronal dynamics of the active region the reader may refer to the article by Zhang & Wang (2001). The SXT images that we present in Figure 3 show the active region before (*bottom left*), during (*bottom middle*), and after (*bottom right*) two filament eruptions that happened west of the active region's main spot on November 4, from 02:22 to 03:46 UT and from 05:17 to 07:17 UT, respectively, and produced two CMEs (Zhang & Wang 2001).

### 3.3. *Active Regions NOAA 9114, 9115, and 9122*

The evolution of these active regions is presented in Figures 5 and 6. On August 6, AR 9114 consists of two positive-polarity sunspots. The main sunspot is the white circular feature in the western part of the field of view of the first few MDI images while the other spot is located northeast of the main spot. The main positive sunspot of AR 9114 shows an outflow of mixed-polarity MMFs from August 5. This outflow is not symmetric; it is stronger in the south-southeastern and western directions (this pattern shows better in Fig. 6, *top left*) and as a result cancellations occur (see the August 6–7 MDI images). At the same time, the small spot moves counterclockwise and approaches the main spot (see Fig. 6, *top right*), and by midday on August 8 the penumbrae of the two spots merge and the spot starts rotating counterclockwise. The sunspot's rotation can be followed until about August 10 (see Fig. 6) and has been studied by Alexander et al. (2002). On August 6–7 converging and shearing motions also happen in AR 9115 (AR 9115 is located close to the center of the field of view of the images in Fig. 5). Furthermore, significant emergence of both positive and negative flux takes place in the northeast part of the field of view of Figure 5. During and after flux emergence the opposite-polarity flux concentrations move away, forming AR 9122. Also note that after midday on August 8, new flux emerges southwest of the main spot of AR 9114.

On August 6–7 LASCO observed two rather faint CMEs associated with activity from AR 9114. On August 9 a geoeffective halo CME occurs, which is associated with a complex eruption (see the EIT images in Fig. 5): a filament eruption occurs between AR 9122 and AR 9115 while flare activity happens in AR 9114. Note that according to the SXT images (Fig. 5) the sigmoid structure of AR 9114 does not erupt; it only dims after the flare (see also Alexander et al. 2002).

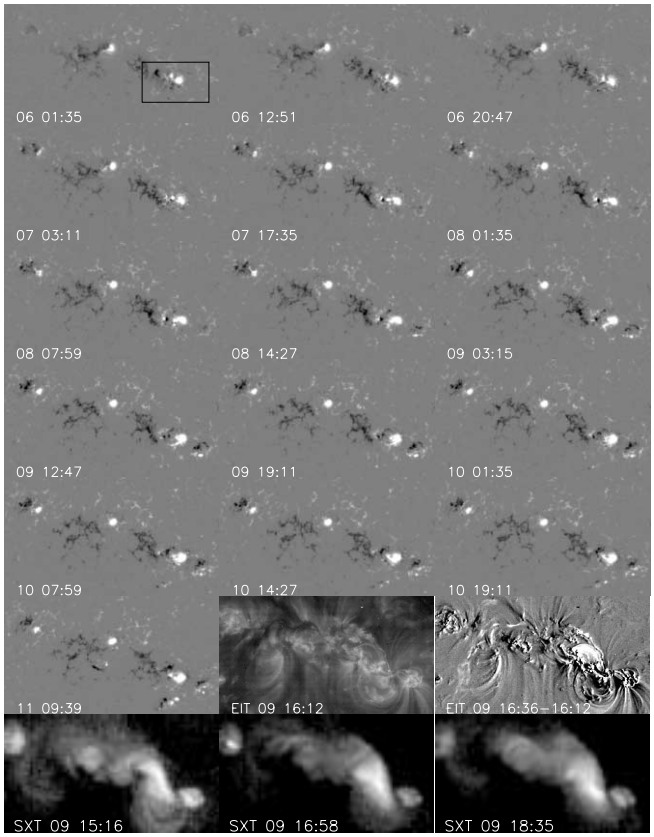


FIG. 5.—Same as Fig. 1 but for the complex of AR 9114, AR 9115, and AR 9122. In the sixth row we show an EIT image of the active region complex obtained on August 9, 16:12 UT and a difference image between the August 9, 16:36 UT EIT image and the August 9, 16:12 UT EIT image. In the bottom row SXT images are presented. The black frame marks the area that appears in Fig. 6.

### 3.4. *Active Region NOAA 9182*

This active region is presented in Figures 7 and 8. During October 6–8 the active region's main sunspot (the intense white feature close to the middle of the field of view of the first MDI images in Fig. 7) exhibits an outflow of mixed-polarity MMFs that show as very small white and black patches around the sunspot in the first few MDI images. From October 9 significant emergence of both positive and negative flux occurs west of the active region's main sunspot. During and after flux emergence the two opposite polarities move away (see Fig. 8). Before this flux emergence, AR 9182 had not produced any CMEs during its disk passage. However, four CMEs (the third is a halo geoeffective CME) associated with AR 9182 are launched within a few hours after the beginning of flux emergence. Furthermore, after October 10 cancellations occur between the positive-polarity plage and negative magnetic elements surrounding it. In Figure 7 we also present SXT images of the active region before and after the geoeffective halo CME showing the sigmoid eruption.

### 3.5. *Active Region NOAA 9201*

We present this active region and the area west of it in Figures 9 and 10. On October 20–22 flux emergence occurs

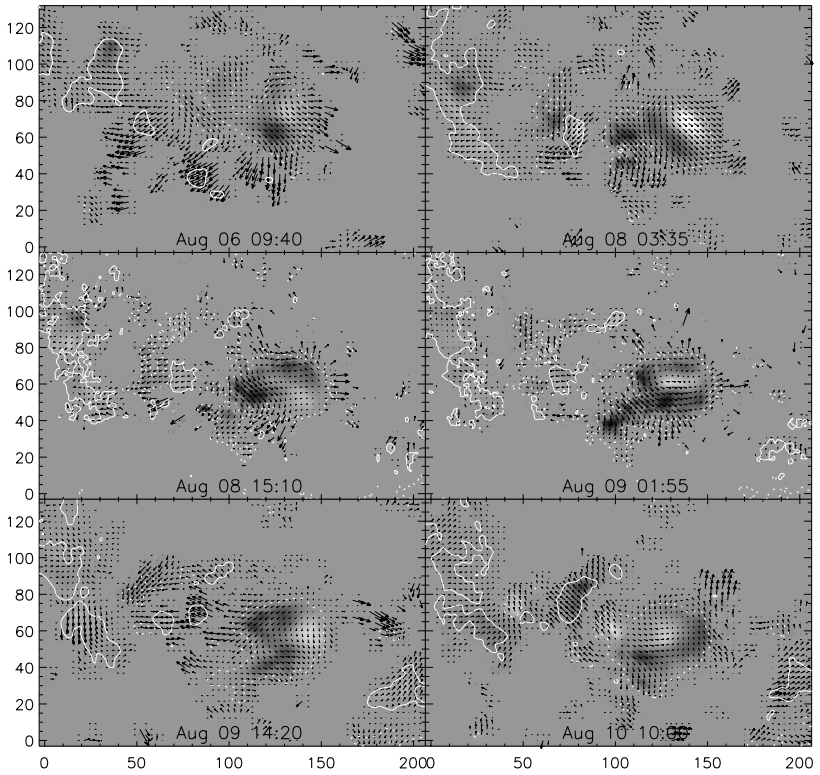


FIG. 6.—Same as Fig. 2 but for AR 9114. The maximum arrow length measures velocity of 0.5 km $s^{-1}$.

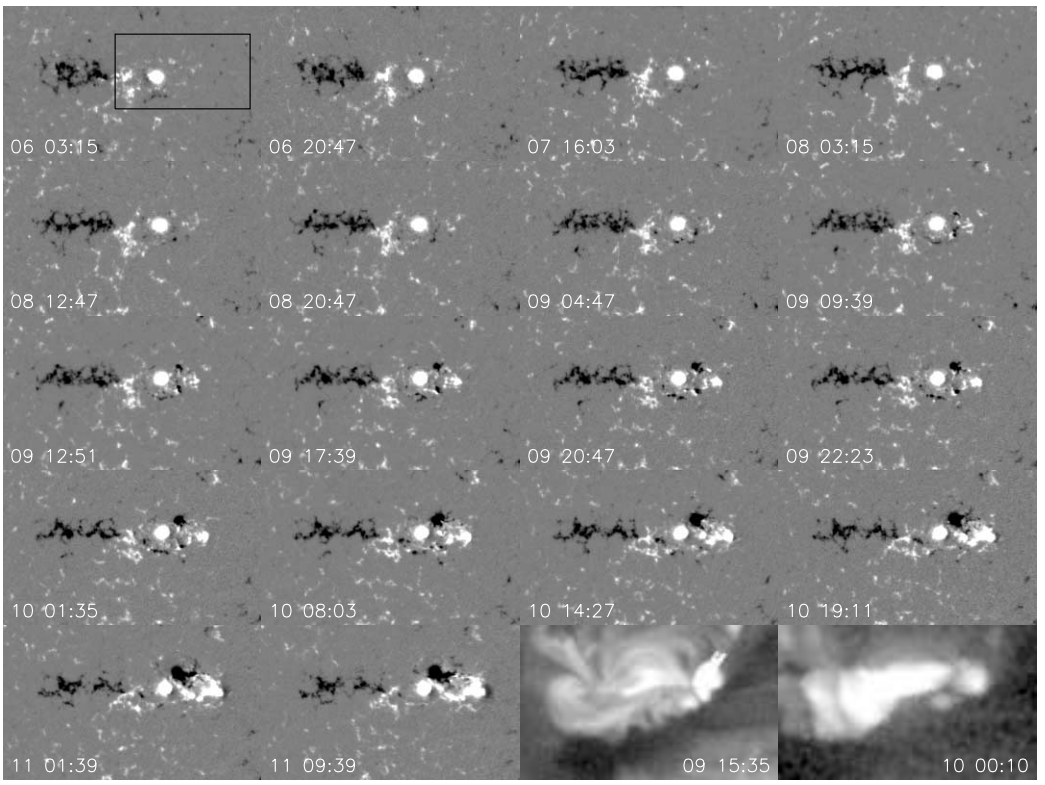


FIG. 7.—Same as Fig. 1 but for AR 9182. The images in the third and fourth columns of the bottom row have been obtained by the SXT. The black frame marks the area that appears in Fig. 8.

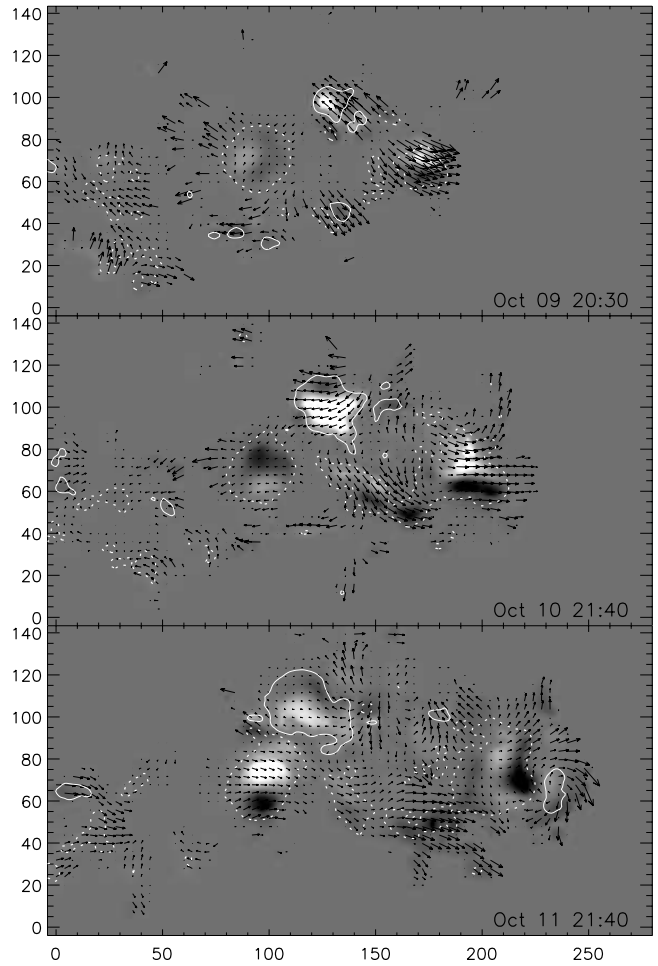


FIG. 8.—Same as Fig. 2 but for AR 9182. The maximum arrow length measures velocity of 0.4 km $s^{-1}$.

in the trailing part of the active region (it appears close to the east central part of the MDI images). The new positive and negative flux concentrations gradually move away (compare the MDI images from October 21, 11:12 UT to October 23, 01:36 UT; this effect also appears in Fig. 10, *top*). From October 22–23 converging motions also occur close to the main neutral line of the active region (see Fig. 10, *middle*), resulting in magnetic flux cancellations, and on October 25 a bipole appears north of the active region's neutral line (see the October 25, 06:27 UT MDI image). Also from early October 21, the two positive-polarity spots in the leading part of the active region start rotating clockwise (see Fig. 10, *top and middle*). The SXT image obtained on October 25, 05:06 UT shows the active region before an eruption that produced a geoeffective CME. The CME first appeared in LASCO images at 08:26 UT. As the middle SXT panel indicates, flare activity started in AR 9201 about half an hour before. The flaring covered a wide region from AR 9201 to the western limb and persisted for several hours.

### 3.6. *Active Regions NOAA 9212, 9213, and 9218*

This complex of active regions is shown in Figure 11. Active regions 9213 and 9212 are located in the southwest and central part, respectively, of the field of view of the images in Figure 11. From October 31 until late on November 2 both shearing and converging motions occur while from October 31 positive- and negative-polarity flux emerges in the northeast part of the field of view. During and after flux emergence these opposite-polarity flux concentrations move away and form AR 9218. On November 1, 21:26 UT a CME first appeared in LASCO images. The CME was associated with activity in the new AR 9218. We also present SXT images of the active region complex. The soft X-ray emission forms a large sigmoidal structure. The leftmost and middle SXT images show the sigmoid several hours and about 3 hours, respectively, before an eruption associated with a geomagnetic CME, while the rightmost image shows the soft X-ray emission after the eruption.

## 4. HELICITY INJECTION COMPUTED WITH THE LCT METHOD

In Figures 12, 13, 14, 15, 16, and 17 we present the temporal variation of the rate of helicity changes $dH/dt|_{\rm LCT}$ (eq. [2]) due to the velocities detected by LCT. We have determined $dH/dt|_{\rm LCT}$ every 5 minutes for the time intervals appearing in Table 1. In the same figures (*bottom*) we show the accumulated change of helicity $\Delta H_{\rm LCT}$ calculated from the measured $dH/dt|_{\rm LCT}$ as a function of time. The time profiles of $dH/dt|_{\rm LCT}$ show (1) large-timescale variations and (2) much shorter irregular fluctuations superposed on the slowly varying component of the helicity injection rate. The spiky component comes from transient localized changes in the computed velocity fields. Chae (2001) has shown that these irregular fluctuations cannot be simply attributed to random errors in velocity computations. Furthermore, Moon et al. (2002a, 2002b) reported six cases of large impulsive variations of helicity change rates associated with M class and X class eruptive flares. Our results show that indeed some impulsive helicity $dH/dt|_{\rm LCT}$ changes are associated with large flares. This shows in Figures 12 and 13, in which we have plotted the corresponding *GOES* soft X-ray flux time profiles. Note that AR 8210 and AR 8375 appeared well before solar maximum, and during their disk passage they produced most of the Sun's flare activity; therefore the flares that appear in the *GOES* plots of Figures 12 and 13 can be attributed to active regions 8210 and 8375, respectively. Note also that in agreement with the results of Moon et al. (2002a, 2002b), sometimes the sign of the impulsive variations of $dH/dt|_{\rm LCT}$ associated with large flares is opposite to that of the smoothly varying component (e.g., the local $dH/dt|_{\rm LCT}$ peaks associated with the two largest flares that came from AR 8210) while sometimes the sign of both components is the same (e.g., the local $dH/dt|_{\rm LCT}$ peak associated with the large flare peak that occurred between 35 and 40 hr in Fig. 13).

However, Figures 12 and 13 show that overall the $dH/dt|_{\rm LCT}$ plots are spikier than the *GOES* plots and sometimes local $dH/dt|_{\rm LCT}$ peaks occur with no significant flaring. In the active regions for which both FD and HR MDI images are available the $dH/dt|_{\rm LCT}$ profiles appear spikier when full-disk MDI images have been used for the helicity injection rate computations. This can be seen by visual inspection of Figures 13, 14, 16, and 17 (compare the morphology of the shaded and nonshaded parts of the top panels of these figures). To quantify this we note that in these active regions the temporal rms values of the derived velocities from FD images are a factor of 1.1–1.5 larger than the temporal rms values of the velocities from HR images

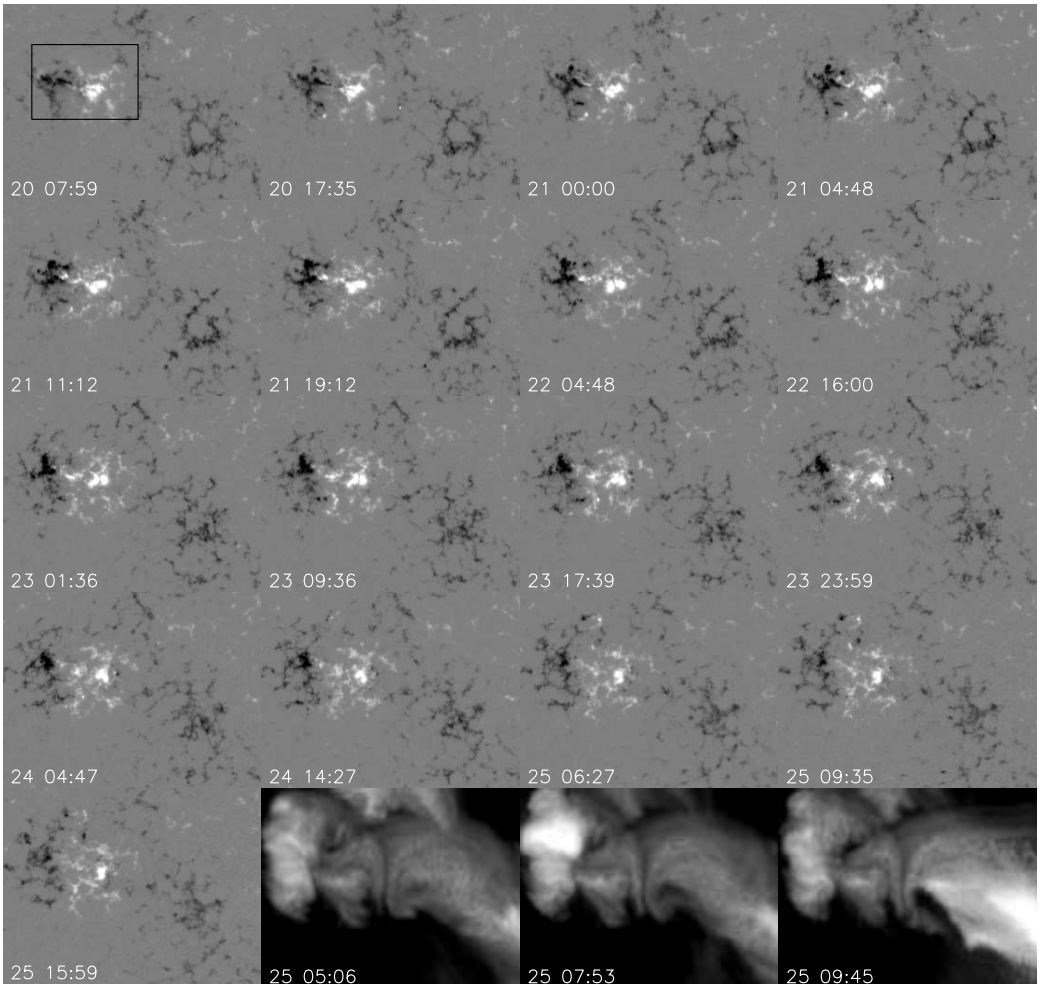


FIG. 9.—Same as Fig. 1 but for AR 9201. The images in the second, third, and fourth columns of the bottom row have been obtained by the SXT. The black frame marks the area that appears in Fig. 10.

(the magnetic field variations are much slower and do not contribute to the spikes in the observed $dH/dt|_{\rm LCT}$ profiles). This effect may imply that at least some impulsive spikes may come from transient localized errors in the velocity computations. In any case, as the figures indicate the time variability of $\Delta H_{\rm LCT}$ is mostly due to the large-timescale trends of the $dH/dt|_{\rm LCT}$ variability. To quantify this we applied a low-pass filter to the $dH/dt|_{\rm LCT}$ profiles by selecting only the modes with periods longer than about 1 hr. For all active regions at the end of the observations the difference between the accumulated change of helicity $\Delta H_{\rm LCT}$ and the resulting $\Delta H$ from the low-pass filtered signal is less than $\pm 4\%$. Therefore our subsequent study will focus on the impact of the large-timescale velocity variations on the corresponding $dH/dt|_{\rm LCT}$ values.

In Figures 2, 4, 6, 8, and 10 we show the computed velocity fields and the corresponding distribution of $G = -2\boldsymbol{v}_{\rm LCT} \cdot \boldsymbol{A}_p B_n$ at selected times (note that the results of the LCT are shown in subregions of the magnetograms only to better show the velocity results; our LCT computations cover the entire field of the view of the magnetograms presented in Figs. 1, 3, 5, 7, 9, and 11). Since we are interested in the large-scale trends of the helicity variability, the velocities and the values of $G$ presented in these images are 1 hr averages around the times indicated in each panel. A brief description of the large-scale flows during the evolution of the active regions has been given in § 3. Here we note that the maxima of the absolute values of the derived velocities are 0.3–0.9 km s$^{-1}$ and the rms values of the derived velocity vectors are 0.1–0.5 km s$^{-1}$. As expected, the figures show that the absolute maxima of the spatial distributions of $G$ correlate well with regions that show intense horizontal motions. To determine whether the computed motions increase or deplete the absolute coronal helicity of the active regions we need to evaluate the chirality of the active regions' magnetic fields. This is done by inspecting the orientation of the transverse component of the photospheric magnetic field by using the HSOS vector magnetograms. We also study visually the orientation of the active regions' coronal structures (as they appear in SXT images) and chromospheric structures (as they appear in Big Bear Solar Observatory full-disk H$\alpha$ images), and in all cases there is agreement with the results derived from the HSOS data. The chiralities of the active regions appear in Table 3.

In all active regions except AR 9201 the accumulated change of helicity $\Delta H_{\rm LCT}$ at the end of the time interval studied is of the same sign as the chirality of the active region. Therefore in five out of six cases at the end of the time intervals studied the computed motions contribute to the increase of the absolute value of the coronal magnetic

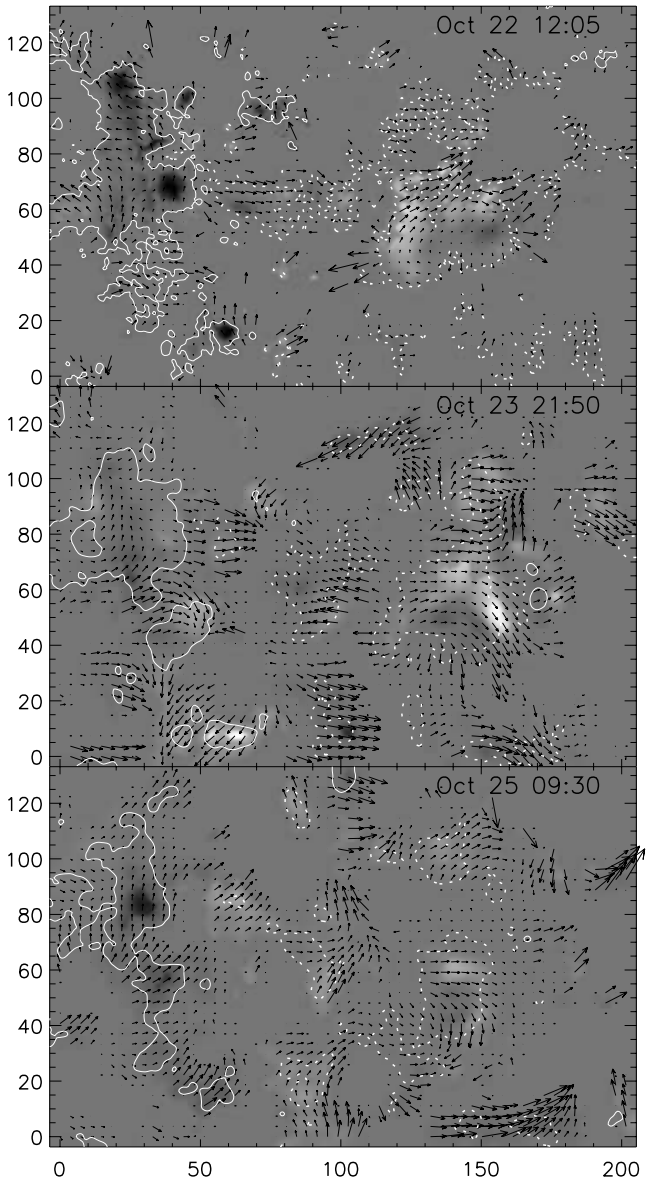


FIG. 10.—Same as Fig. 2 but for AR 9201. The maximum arrow length measures velocity of 0.3 km $s^{-1}$.

field helicity. However, cancellation of helicity injected at different locations of each active region occurs (i.e., positive and negative helicity changes may be mixed in an active region) and can be seen in the figures, in the images of $G$, for all cases we studied. Furthermore, in several cases the sign of the slowly varying component of $dH/dt|_{\rm LCT}$ changes during the observations. These effects have been also observed by Chae (2001) and Nindos & Zhang (2002).

The computed motions associated with helicity injection that increases the absolute value of the coronal magnetic field helicity appear as twisting and/or shearing motions. The contribution of twisting motions shows well in Figures 2 and 6, in which the sunspots of AR 8210 (region having positive chirality) and AR 9114 (region having negative chirality) rotate clockwise and counterclockwise, respectively. In AR 8375 (Fig. 4) the sunspot does not rotate (at least for most of the time interval studied) but moves westward. A purely westward motion of a symmetric sunspot of

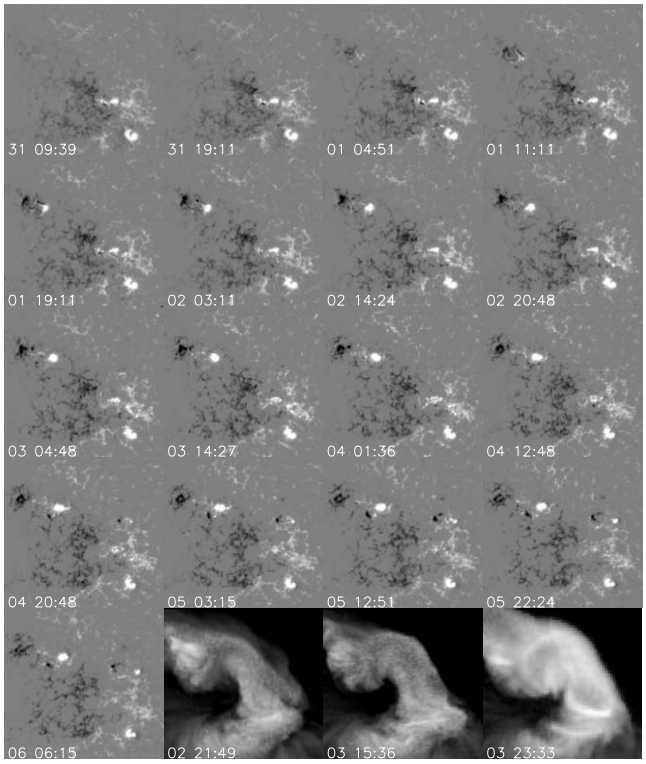


FIG. 11.—Same as Fig. 9 but for the complex of AR 9212, AR 9213, and AR 9218.

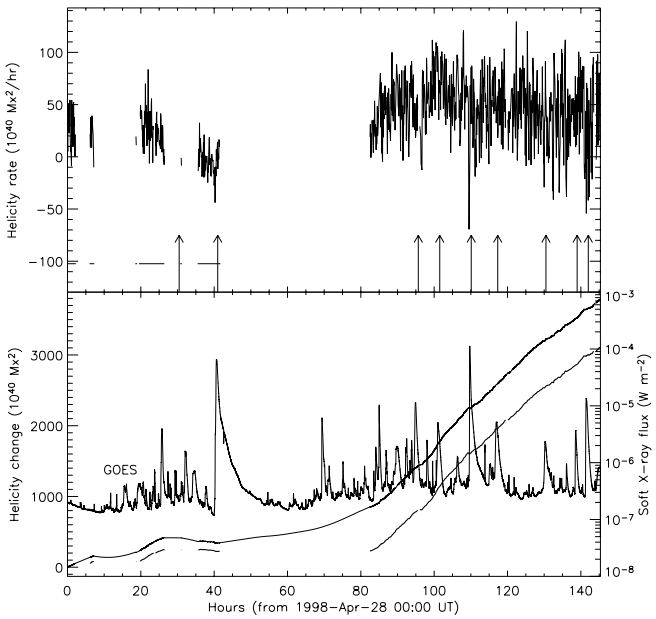


FIG. 12.—*Top*: Time profile of $dH/dt|_{\rm LCT}$ in AR 8210. The arrows indicate the time of the first appearance in the LASCO images of the CMEs originated from the active region. The horizontal lines indicate the time intervals when 1 minute cadence white-light MDI images were available. *Bottom*: Time profile of the accumulated change of helicity $\Delta H(t)$ calculated from the measured $dH/dt$ (*thick line*) and the estimated $\Delta H(t)$ if a spline interpolation is used for the determination of the missing $dH/dt$ values (*thin line*). Here and in Fig. 13 we also present the *GOES* soft X-ray flux time profile.

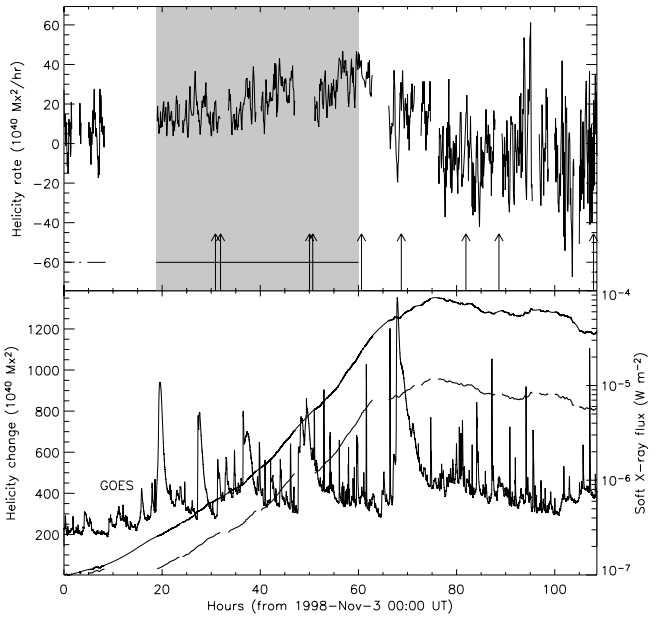


FIG. 13.—Same as Fig. 12 but for AR 8375. In this and subsequent figures the shaded areas indicate the time intervals when HR images have been used.

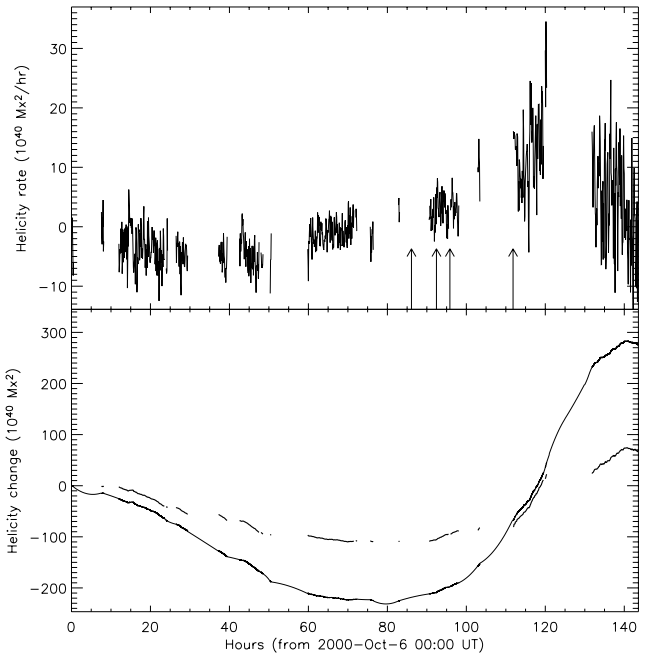


FIG. 15.—Same as Fig. 12 but for AR 9182

a given polarity is expected to give no net helicity injection because $G$ has opposite sign contribution in its northern and southern part. Therefore the bulk of the net helicity injection in AR 8375 rather comes from deviations from such motion. These deviations are associated with shearing motions of the sunspot with respect to opposite flux concentrations, polarity deformations, and asymmetries in $B_n$ repartition. In AR 9182 (Fig. 8) the coronal helicity increases because of motions occurring during and after flux emergence: the newly emerged opposite polarities move away such that a component of their velocity vectors is parallel to the polarity inversion line. But this effect is localized, spatially incoherent, and does not last more than 25 hr; therefore the contribution of the computed motions to the increase of the coronal helicity is small (see Fig. 15). A similar situation happens in the complex of AR 9212, AR 9213, and AR 9218 (for the sake of brevity no velocity field is presented). In AR 9201 (region having negative chirality) the clockwise rotation of two sunspots depletes helicity from the coronal magnetic field.

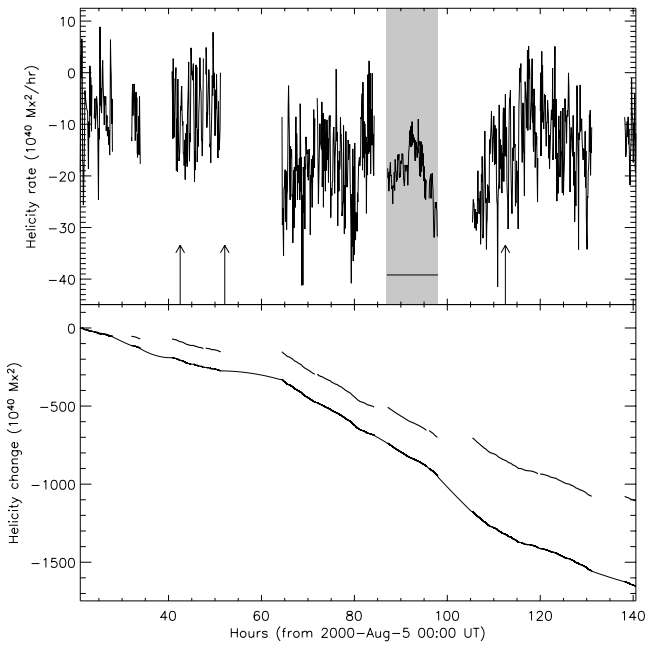


FIG. 14.—Same as Fig. 12 but for the complex of AR 9114, AR 9115, and AR 9122.

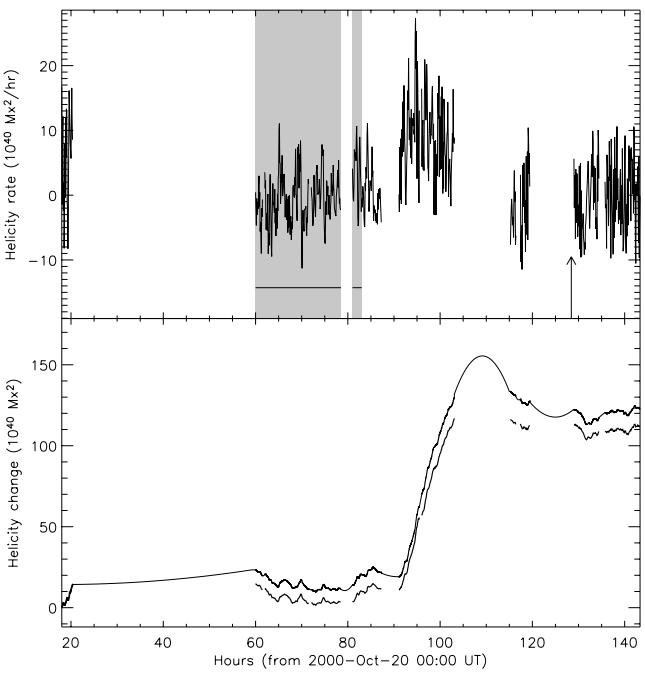


FIG. 16.—Same as Fig. 12 but for AR 9201

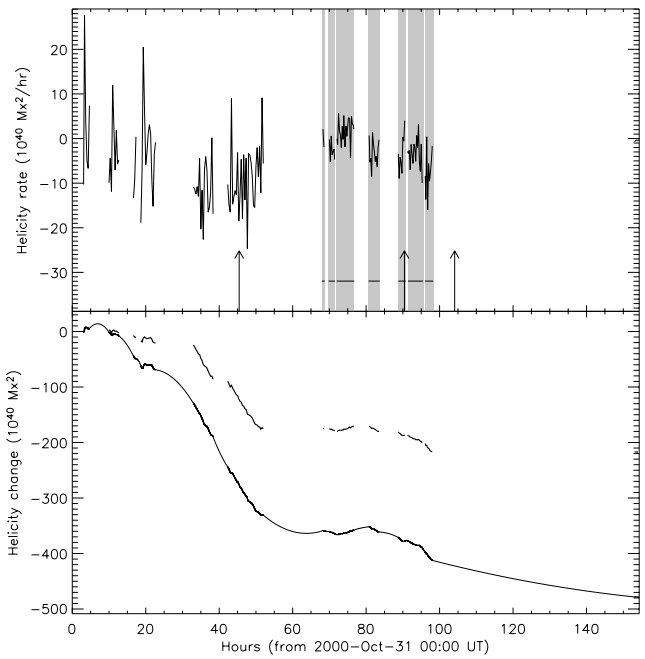


FIG. 17.—Same as Fig. 12 but for the complex of AR 9212, AR 9213, and AR 9218.

## 5. HELICITY BUDGET OF THE ACTIVE REGIONS

In Figures 12, 13, 14, 15, 16, and 17 the arrows mark the time of the first appearance of the CMEs linked to the active regions in the LASCO images. These CMEs are identified in full-disk EIT images using as proxies the presence of dimmings and/or expanding loops. The helicity carried away by CMEs cannot be directly computed. To overcome this problem we follow the method used by Démoulin et al. (2002b) and Nindos & Zhang (2002). Démoulin et al. (2002b) assumed that each CME ejected from the active region they studied produced an MC. Then one assumes that the helicity carried away by each CME is equal to the helicity in the corresponding MC. The magnetic helicity per unit of length in an MC can be calculated if we know the axial magnetic field $B_0$ and the radius $R$ of the cloud's flux rope (DeVore 2000; see his eq. [49]). These parameters can be calculated using a magnetic field model (Lepping, Burlaga, & Jones 1990) that assumes that the magnetic field within the MC is described by the first harmonic of a linear force-free field.

All active regions presented in this paper are associated with halo CMEs that produce MCs observed by *Wind* spacecraft (see § 2). Each active region is associated with only one MC. The values of $B_0$ and $R$ that correspond to the best-fit models of Lepping et al. (1990) to these MCs have been taken from the *Wind* web page.[1] These model fits have been judged to be excellent (for the MCs associated with AR 9114 and AR 9182) or good (for the MCs associated with AR 8210, 8375, and 9213), and only the model fit to the MC associated with AR 9201 has been judged to be poor. To calculate the total helicity in the MC we need the length $l$ of the cloud's flux tube. In this study we assume a uniform distribution of twist along the MC. Since the true $l$ cannot be obtained observationally, we will consider three different sets of $l$. First we assume that the MCs are still connected to the Sun when observed at 1 AU and therefore $l \sim 2$ AU (see Démoulin et al. 2002b, and references therein). Then the resulting MC helicities are given in column (2) of Table 2. These values may be considered upper limits to the MC helicities.

A different method for the determination of $l$ can be applied by using the fact that cylindrical line-tied force-free loops have been found to be kink-unstable when a critical twist is exceeded. Then the resulting critical helicity of the twisted flux rope having $n_k$ turns and axial flux $F$ is given by $H_k = n_k F^2$. Several important papers exist on the kink instability but the values do not converge to a single critical twist value even with initial symmetric cylindrical configurations (Hood & Priest 1979; Rust & Kumar 1996; Galsgaard & Nordlund 1997; Baty 1997, 2001). For example Hood & Priest (1979) show that the instability threshold lies at $n_k = 1.25$ while Rust & Kumar (1996) derive a critical value of $n_k = 1.85$. On the other hand Baty (1997) shows that $n_k$ may range from 2.25 to 4.25, depending on the aspect ratio of the loop. Furthermore, these results are for initial configurations that are cylindrically symmetric, and therefore the application of these results to active region fields is far from being straightforward. Here we adopt a critical value of

[1] See http://lepmfi.gsfc.nasa.gov/mfi/mag_cloud_pub1.html.

TABLE 2
PROPERTIES OF MAGNETIC CLOUDS

| NOAA Active Region (1) | $H_{MC}$[a] ($\times 10^{40}$ Mx$^2$) (2) | $F_{MC}$[b] ($\times 10^{20}$ Mx) (3) | $H_k$[c] ($\times 10^{40}$ Mx$^2$) (4) | $l_k$[d] (AU) (5) |
|---|---|---|---|---|
| 8210 | 1844 | 22.7 | 1030 | 1.1 |
| 8375 | 492 | 8.5 | 144 | 0.6 |
| 9114 | −1904 | 18.5 | −684 | 0.7 |
| 9182 | 294 | 7.1 | 101 | 0.7 |
| 9201 | −2980 | 31.0 | −1922 | 1.3 |
| 9213 | −1194 | 14.4 | −415 | 0.7 |

[a] MC helicity using $l = 2$ AU.
[b] MC absolute axial flux.
[c] MC helicity using eq. (5).
[d] Length of an MC flux tube containing helicity $H_k$.

about $n_k \approx 2$, and therefore we have

$$H_k \approx 2F^2 \ . \quad (5)$$

However, we do not want to give the false impression that the kink instability will occur in an active region for a well-known number of turns. Moreover, recent studies (Leamon et al. 2003) indicate that it is not clear at all whether the kink instability is the eruption mechanism. However, our use of equation (5) is justified given the large uncertainties in the MC length and helicity estimations.

DeVore (2000) has shown that the axial flux $F_{\rm MC}$ of an MC is $F_{\rm MC} = 1.4|B_0|R^2$. For each MC we calculate $F_{\rm MC}$ by using again the values of $B_0$ and $R$ derived from the Lepping et al. (1990) best-fit model (note that except AR 9201 the derived values of $F_{\rm MC}$ agree within $\pm 20\%$ with the photospheric flux computed over the EIT dimming regions associated with the halo geoeffective CMEs). Then equation (5) gives an independent estimate, $H_k$, for the MC helicity. The values of $H_k$, together with the resulting values of $l_k$, appear also in Table 2. We note, however, that the derived values of $H_k$, and so of $l_k$, are also uncertain (see the above discussion). A third way to get $l$ is to follow DeVore (2000), who suggested that $l = 0.5$ AU. In such case the resulting MC helicities are 1/4 of the values presented in Table 2 column (2) and should be considered lower limits to the MC helicities.

The contribution of differential rotation to the helicity budget of the active regions is estimated by introducing the differential rotation at the place of the velocities given by LCT and computing the corresponding helicities $dH/dt|_{\rm rot}$ in the same way. The resulting accumulated helicity due to differential rotation $\Delta H_{\rm rot}$ during each time interval used in our study is given in Table 3. In AR 9201 differential rotation increases the (absolute) coronal helicity, contrary to the other computed motions. In this active region and in the complex of AR 9212, 9213, and 9218 the accumulated helicity due to differential rotation is a factor of 3.2 and 1.4, respectively, higher than the absolute value of the accumulated helicity due to the other computed motions. In the other active regions the relative contribution of differential rotation is small.

In Table 3 we also give the accumulated helicity $\Delta H_{\rm LCT}$ computed with the LCT method (other than differential rotation), the number of CMEs associated with the active region, and the total helicity carried away by the CMEs, by using the three different values of $l$. The CME helicities derived with $l = 2$ AU are a factor of 2.9–10.1 higher than the total helicity accumulated by both the computed horizontal motions and differential rotation. The larger helicity deficit is associated with AR 9201; we remind the reader, however, that in the MC associated with AR 9201 the best-fit $B_0$ and $R$ have been judged to be poor. For the remaining active regions the CME helicities are a factor of 2.9–4 higher than the total helicity accumulated by both the computed transient motions and differential rotation. The CME helicities determined with $l$ derived from equation (5) and $l = 0.5$ AU are broadly consistent with the sums of $\Delta H_{\rm LCT} + \Delta H_{\rm rot}$ (again with the exception of AR 9201). This picture shows better in columns (9)–(11) in Table 3, in which we give the helicity deficit between the CMEs and all computed motions.

Our calculations assume that in each active region all CMEs eject the same amount of helicity, which is equal to the helicity of the MC associated with the active region. Considering the variety of CME sizes, speed, and morphology the corresponding CME helicities in a given active region may be different. Therefore we have repeated the helicity budget calculations assigning the MC helicities presented in Table 2 only to the corresponding halo CMEs. The helicity of the nonhalo CMEs have been calculated using the average $B_0$ and $R$ values used by DeVore (2000). Assuming $l = 2$ AU we find that the helicity injected by all computed motions should be multiplied by factors of 2.8, 3.8, 1.8, 8.6, and 2.4 for AR 8210, 8375, 9114, 9182, and 9213, respectively, to match the total helicity ejected by the CMEs. If we use the values of $l_k$ given in Table 2 and $l = 0.5$ AU these factors become 1.4–0.7, 1.0–1.0, 0.6–0.4, 2.6–2.2, and 0.7–0.6 for the above active regions (in each of these pairs the first number corresponds to $l = l_k$ and the second to $l = 0.5$ AU). In these calculations the largest helicity deficit in favor of the CMEs appears in AR 9182 because the values of $B_0$ and $R$ used by DeVore (2000) are larger than the values of $B_0$ and $R$ derived from the best-fit model of the active region MC.

Several flux emergence episodes have occurred during our observations (see § 3). But even a lack of significant increase

TABLE 3
HELICITY BUDGETS

| NOAA Active Region (1) | $\alpha_{\rm AR}$ [a] (2) | $\Delta H_{\rm LCT}$ ($\times 10^{40}$ Mx$^2$) (3) | $\Delta H_{\rm rot}$ ($\times 10^{40}$ Mx$^2$) (4) | CMEs (5) | $H^{\rm tot}_{\rm CME}$ [b] ($\times 10^{40}$ Mx$^2$) $l = 2$ AU (6) | $l = l_k$ (7) | $l = 0.5$ AU (8) | $(H^{\rm tot}_{\rm CME} - \Delta H_{\rm LCT} - \Delta H_{\rm rot})/H^{\rm tot}_{\rm CME}$ [c] (%) $l = 2$ AU (9) | $l = l_k$ (10) | $l = 0.5$ AU (11) |
|---|---|---|---|---|---|---|---|---|---|---|
| 8210 | + | 3784 | 324 | 9 | 16596 | 9270 | 4149 | 75 | 56 | 1 |
| 8375 | + | 1178 | 334 | 9 | 4428 | 1296 | 1107 | 65 | −17 | −36 |
| 9114, 9115, 9122[d] | − | −1697 | −257 | 3 | −5712 | −2052 | −1428 | 66 | 5 | −37 |
| 9182 | + | 276 | 34 | 4 | 1176 | 404 | 294 | 74 | 23 | −5 |
| 9201 | − | 133 | −428 | 1 | −2980 | −1922 | −745 | 90 | 84 | 60 |
| 9212, 9113, 9118[d] | − | −477 | −666 | 3 | −3582 | −1245 | −895 | 68 | 8 | −28 |

[a] Active region's chirality.

[b] Cols. (6)–(8) refer to the total helicity ejected by the CMEs derived using $l = 2$ AU, eq. (5), and $l = 0.5$ AU, respectively, for the MC helicity computation.

[c] In cols. (9)–(11) the total helicity ejected by the CMEs has been derived using $l = 2$ AU, eq. (5), and $l = 0.5$ AU, respectively, for the MC helicity computation.

[d] The values of $\Delta H_{\rm LCT}$ and $\Delta H_{\rm rot}$ refer to the whole complex of active regions.

of vertical flux does not necessarily mean that there is no contribution of emerging flux to the helicity injected into the corona (Démoulin et al. 2002b; Green et al. 2002). Unfortunately a direct computation of the helicity injected by flux emergence is not possible (e.g., Démoulin & Berger 2003, but see Kusano et al. 2002). The implications of our results concerning the helicity injected by flux emergence will be discussed in the remaining sections of the paper. Furthermore, we do not attempt to compute the change of coronal helicity during our observations because (1) the active regions complexes that we study show complicated coronal morphology and it is highly unlikely that a linear force-free magnetic field model would be able to model the coronal magnetic field reliably and (2) the uncertainties in the helicities concerning CMEs and computed motions are significant (see also § 6).

## 6. UNCERTAINTIES IN THE HELICITIES COMPUTED WITH THE LCT METHOD

For the computation of the helicity injected by both the observed transient horizontal motions and differential rotation we have used MDI longitudinal magnetic field data after we corrected them to compensate for their underestimation of magnetic field fluxes and saturation (see § 2.2). These correction factors make the helicities presented in this paper higher by factors of 2.38–2.59 with respect to the helicities that would have been computed without the application of the MDI correction factors.

There are also serious issues concerning the use of LCT for the computation of the horizontal velocities. When there is both flux emergence and transient horizontal motions, part of each horizontal velocity vector computed by the LCT method comes from the process of flux emergence. This issue has been studied in detail by Démoulin & Berger (2003). Here we follow their analysis and consider a magnetic flux tube that is transported ideally by plasma motions across the photosphere with only a normal velocity component $v_n$ (the plasma velocity is $v_t = 0$). Then as Démoulin & Berger (2003) show (see their Fig. 1 and their eq. [21]) the photospheric footpoints of the field lines are moving on the photosphere with a tangential velocity

$$\boldsymbol{v}_f = -\frac{v_n}{B_n}\boldsymbol{B}_t \ . \tag{6}$$

Then the LCT method will detect a tangential velocity $v_t = v_f$ despite the fact that we have assumed that the plasma velocity is $v_t = 0$. Therefore, when we have both flux emergence and transient horizontal motions (i.e., $v_t \neq 0$) the LCT will detect a velocity of $\boldsymbol{v}_t - (v_n/B_n)\boldsymbol{B}_t$. If we insert this expression for the velocity in equation (2) we get the whole helicity flux (see eqs. [2] and [3]), within the accuracy of the LCT method. This indicates, as Démoulin & Berger (2003) have proved, that the helicity flux computed using LCT velocities includes both the contribution of horizontal and vertical plasma flows; i.e., the helicity flux coming from flux emergence is included in the LCT computation!

Furthermore, the LCT method has other serious limitations that lead to underestimation of the computed helicities. First, the low spatial resolution of present magnetograms limits the obtained velocities to the velocity of group motion of the unresolved bunch of thin ($\leq$100 km) flux tubes covered by a given pixel. Related to this problem is the lower resolution of the FD magnetograms with respect to the resolution of the HR magnetograms: in all active regions for which both FD and HR MDI images are available the time profiles of $dH/dt|_{\rm LCT}$ appear spikier when they come from full-disk magnetograms (see the discussion in § 4). Twisting motions along the isocontours of $B_n$ cannot be detected by the LCT method (see Démoulin & Berger 2003). An intrinsic problem related to the LCT method is the optimal choice of the parameters $\Delta T$ and $w$, which prevents tracking of fast motions and has a smoothing effect on the velocities because the correlated subareas are typically 2–5 times larger than the spatial resolution of the magnetogram.

LCT may face significant difficulties in regions such as sunspot umbrae where the field distribution has small spatial variation and hence the data do not provide enough information to follow individual flux tubes. This is the reason that we used white-light images (when they were available) and not magnetograms for the computation of velocity fields in the umbrae and penumbrae of sunspots. The velocities derived from the application of the LCT method on white-light images are up to 10%–20% higher than the velocities derived from LCT on the corresponding simultaneous magnetograms. For the active regions where white-light images are available, at the end of the observations the accumulated change of helicity computed using white-light images is less than 3%–5% higher than the accumulated change of helicity computed using magnetograms only (note that in the time intervals we studied the white-light image coverage is poorer compared with the magnetogram coverage; see Figs. 12, 13, 14, 16, and 17).

Other possible sources of error are introduced by the computed $B_n$ and $\boldsymbol{v}_{\rm LCT}$ away from disk center. Using the HSOS transverse field images we find that the simple $B_n$ model used in the calculations does not introduce errors in the $dH/dt$ computations larger than about 15%. Chae et al. (2001) have studied possible fake motions introduced by errors in $\boldsymbol{v}_{\rm LCT}$ due to projection effects. Following their analysis we find that such errors are localized and do not affect our results more than $\pm$10%.

## 7. CONCLUSIONS

In this paper we have studied the photospheric magnetic field evolution of six active regions that were associated with halo CMEs that produced MCs observed by *Wind* spacecraft at 1 AU. The main purpose of our study was the study of the helicity budget of active regions by comparing the helicity injected by the photospheric motions computed with the LCT method with the helicity carried away by CMEs. The rate of helicity change due to the computed motions other than differential rotation has been estimated for about 110–150 hr when the active regions were not close to the limb. The time profiles of $dH/dt|_{\rm LCT}$ show large-timescale variations and also much shorter irregular fluctuations superposed on the slowly varying component. The time variability of the accumulated change of helicity $\Delta H(t)_{\rm LCT}$ comes primarily from the large-timescale trends of the $dH/dt|_{\rm LCT}$ variability, and therefore our study did not focus on the irregular fluctuations (some of them are associated with large flares but others may be due to transient localized errors in the velocity computations).

In five of the six active regions the accumulated $\Delta H_{\rm LCT}$ at the end of the time intervals studied is of the same sign as

the chirality of the active region, and therefore in these active regions the computed photospheric motions contribute to the increase of the absolute value of the coronal magnetic field helicity. In two active regions the accumulated helicity due to differential rotation is a factor of 3.2 and 1.4 higher than the absolute value of the accumulated helicity due to the other computed motions. In the other active regions the relative contribution of differential rotation is much smaller than the contribution from the other motions. The most efficient helicity-producing photospheric flows include the shearing component of the motion of a fast-moving sunspot (AR 8375) and rotating sunspots (AR 8210 and AR 9114). The sunspot rotation increases the absolute coronal helicity when it is counterclockwise in active regions having negative chirality and clockwise in regions having positive chirality.

With the LCT method we follow the photospheric location of magnetic flux tubes, not the plasma; this implies that the helicities computed from LCT velocities include both the contribution from horizontal and vertical plasma flows (Démoulin & Berger 2003; also see § 6). The helicity coming from flux emergence is included in the computations presented in this paper, and therefore the sums $\Delta H_{\rm LCT} + \Delta H_{\rm rot}$ appearing in Table 3 should be regarded as the total accumulated helicity injected into the corona from all possible mechanisms (i.e., shearing or twisting motions, emerging flux, and differential rotation).

In the light of the above arguments one would expect that the deficit between the computed $\Delta H_{\rm LCT} + \Delta H_{\rm rot}$ and the helicities carried away by the CMEs linked to a given active region would have been small. We suggest that the deficits indicate the uncertainties in the MC helicity calculations and the limitations of the LCT method. Our database contains MCs associated with CMEs linked to our active regions and therefore direct information about the helicity *per unit of length* in the corresponding twisted interplanetary flux tubes is provided. However, the computation of the total helicity carried away by the CMEs associated with any of our active regions is subject to significant uncertainties because (1) we do not know the length $l$ of the MC flux tube, (2) we do not know whether all CMEs carry away the same amount of helicity, and (3) we do not know the distribution of twist along the MC flux tube. We assume that in a given active region each CME carries away the same amount of helicity, which is determined by the helicity of the MC linked to the active region. For each MC three different helicity values were derived, corresponding to $l = 2$ AU, $l = 0.5$ AU, and $l$ determined by the condition for the initiation of the kink instability in the coronal flux rope. The total CME helicities derived with $l = 2$ AU are a factor of 2.9–4 higher than the total helicity injected into the corona. If we use $l = 0.5$ AU or the values of $l$ derived by equation (5) then the total CME helicities and the total helicities injected into the corona are broadly consistent (we do not take into account AR 9201, for which the MC force-free model is poor).

The discrepancies between the helicities carried away by the CMEs and the total helicities injected into the corona as computed using the LCT method point out not only the uncertainties in the MC/CME calculations but also the limitations of the LCT method. As we noted in § 6 the LCT method underestimates the computed helicities. This effect can be demonstrated in an independent way if we express the accumulated values of $\Delta H_{\rm LCT} + \Delta H_{\rm rot}$ presented in Table 3 in units of $\Phi^2$, where $\Phi$ is the active region's magnetic flux (see Table 1). Then we get that the total accumulated helicities are between 0.007 and 0.17. These values are below the theoretical upper limit for the total helicity derived by spatially and temporally coherent shearing motions (Démoulin et al. 2002a). On the other hand, however, recently Leamon et al. (2003) demonstrated that the total twist of coronal sigmoids may be much less than one turn.

We believe that our study, at least partially, clears up some of the discrepancies in the helicity budget of active regions because the discrepancies appearing in the present study are probably smaller than previous discrepancies reported by Démoulin et al. (2002b) and Nindos & Zhang (2002). In the previous studies there was a larger deficit of about a factor of at least 10 of photospheric helicity flux when the MC/CME helicity calculation was done with $l = 2$ AU and a factor of more than 2.5 when the MC/CME helicity was done with $l = 0.5$ AU (these numbers result after correction for MDI flux underestimation).

The improvement of photospheric measurements of $\boldsymbol{B}$ and $\boldsymbol{v}$ will help us determine the helicity injected into the corona more accurately. Concerning the MC/CME helicity we need to constrain more accurately the length of MC flux tubes and investigate whether the twist along an interplanetary flux tube is uniform. The latter task could be performed by the anticipated *STEREO* mission if an MC would pass by two *STEREO* spacecraft.

A. N. would like to thank C. E. Alissandrakis for reading the manuscript and for his encouragement and P. Démoulin for sending him the first submitted version of his latest paper on magnetic helicity. He also thanks Jeneen Sommers and Jim Aloise for their practical help. J. Z. acknowledges support from NASA contract NRA-01-01-SSS-073 and NSF award ATM-0203226. We thank the referee for his or her valuable comments, which led to significant improvement of the paper. This research has used the CME catalog that is generated and maintained by NASA and the Catholic University of America in cooperation with the NRL. *SOHO* is a project of international cooperation between ESA and NASA.

## REFERENCES

Ai, G. X., & Hu, Y. F. 1986, Acta Astron. Sinica, 27, 173
Alexander, D., Nightingale, R., Metcalf, T. R., & Brown, D. 2002, BAAS, 200, 36.08
Baty, H. 1997, A&A, 318, 621
———. 2001, A&A, 367, 321
Berger, M. A. 1988, A&A, 201, 355
———. 1999, in Magnetic Helicity in Space and Laboratory Plasmas, ed. M. R. Brown, R. C. Canfield, & A. A. Pevtsov (Geophys. Monogr. 111; Washington: AGU), 1
Berger, T. E., & Lites, B. W. 2003, Sol. Phys., 213, 213
Canfield, R. C., Hudson, H. S., & McKenzie, D. E. 1999, Geophys. Res. Lett., 26, 627
Chae, J. 2001, ApJ, 560, L295
Chae, J., Wang, H., Qiu, J., Goode, P. R., Strous, L., & Yun, H. S. 2001, ApJ, 560, 476
Chen, J. 1996, J. Geophys. Res., 101(A12), 27499
Démoulin, P., & Berger, M. A. 2003, Sol. Phys., in press
Démoulin, P., Mandrini, C. H., van Driel–Gesztelyi, L., Lopez-Fuentes, M. C., & Aulanier, G. 2002a, Sol. Phys., 207, 87
Démoulin, P., Mandrini, C. H., van Driel–Gesztelyi, L., Thompson, B. J., Plunkett, S., Kövari, Zs., Aulanier, G., & Young, A. 2002b, A&A, 382, 650
DeVore, C. R. 2000, ApJ, 539, 944
Feynman, J., & Martin, S. F. 1995, J. Geophys. Res., 100, 3355

Forbes, T. G., & Priest, E. R. 1995, ApJ, 446, 377
Forbes, T. J. 2000, J. Geophys. Res., 105(A10), 23153
Galsgaard, K., & Nordlund, Å. 1997, J. Geophys. Res., 102, 219
Gosling, J. T. 1993, J. Geophys. Res., 98(A11), 18937
Green, L. M., Démoulin, P., Mandrini, C. H., & van Driel–Gesztelyi, L. 2003, Sol. Phys., in press
Green, L. M., Lopez Fuentes, M. C., Mandrini, C. H., Démoulin, P., van Driel–Gesztelyi, L., & Culhane, J. L. 2002, Sol. Phys., 208, 43
Harvey, K., & Harvey, J. 1973, Sol. Phys., 28, 61
Hood, A. W., & Priest, E. R. 1979, Sol. Phys., 64, 303
Hudson, H. S., & Cliver, E. W. 2001, J. Geophys. Res., 106, 25199
Khan, J. I., & Hudson, H. S. 2000, Geophys. Res. Lett., 27, 1083
Klimchuk, J. A. 2000, in Proc. Chapman Conf. on Space Weather, ed. P. Song, G. Siscoe, & H. Singer (Washington: AGU)
Kusano, K., Maeshiro, T., Yokoyama, T., & Sakurai, T. 2002, ApJ, 577, 501
Lara, A., Gopalswamy, N., & DeForest, C. 2000, Geophys. Res. Lett., 27, 1435
Leamon, R. J., Canfield, R. C., Blehm, Z., & Pevtsov, A. A. 2003, ApJ, submitted
Leka, K. D., Canfield, R. C., McClymont, A. N., & van Driel–Gesztelyi, L. 1996, ApJ, 462, 547
Lepping, R. P., Burlaga, L. F., & Jones, J. A. 1990, J. Geophys. Res., 95, 11957
Mikić, Z., & Linker, J. A. 1994, ApJ, 430, 898
Moon, Y.-J., Chae, J., Wang, H., Choe, G. S., & Park, Y. D. 2002a, ApJ, 580, 528
Moon, Y.-J., et al. 2002b, ApJ, 574, 1066
Nindos, A., Alissandrakis, C. E., Gelfreikh, G. B., Bogod, V. M., & Gontikakis, C. 2002, A&A, 386, 658
Nindos, A., & Zhang, H. 2002, ApJ, 573, L133
Nindos, A., & Zirin, H. 1998, Sol. Phys., 182, 381
November, L. J., & Simon, G. W. 1988, ApJ, 333, 427
Pohjolainen, S., et al. 2001, ApJ, 556, 421
Rust, D. M. 1983, Space Sci. Rev., 34, 21
Rust, D. M., & Kumar, A. 1996, ApJ, 464, L199
Sheeley, N. R., Jr., et al. 1975, Sol. Phys., 45, 377
Sterling, A. C., & Hudson, H. S. 1997, ApJ, 491, L55
Sterling, A. C., & Moore, R. L. 2001, ApJ, 560, 1045
Sterling, A. C., Moore, R. L., Qiu, J., & Wang, H. 2001, ApJ, 561, 1116
Subramanian, P., & Dere, K. P. 2001, ApJ, 561, 372
Thompson, B. J., Cliver, E. W., Nitta, N., Delanee, C., & Delaboudiniere, J.-P. 2000, J. Geophys. Res., 25, 2465
Thompson, B. J., Plunkett, S. P., Gurman, J. B., Newmark, J. S., St. Cyr, O. C., & Michels, D. J. 1998, Geophys. Res. Lett., 25(14), 2465
van Driel–Gesztelyi, L., et al. 1999, in ASP Conf. Ser. 184, Third Advances in Solar Physics Euroconference: Magnetic Fields and Oscillations, ed. B. Schmieder, A. Hofmann, & J. Staude (San Francisco: ASP), 302
Wang, H., et al. 2000, ApJ, 536, 971
Wang, T., & Abramenko, V. I. 2000, A&A, 357, 1056
Wang, T., Yan, Y., Wang, J., Kurokawa, H., & Shibata, K. 2002, ApJ, 572, 580
Wang, T. J., Ai, G. X., & Deng, Y. Y. 1996, Publ. Beijing Astron. Obs., 28, 31
Warmuth, A., Hanslmeier, A., Messerotti, M., Cacciani, A., Moretti, P. F., & Otruba, W. 2000, Sol. Phys., 194, 103
Yurchyshyn, V. B., & Wang, H. 2001a, Sol. Phys., 202, 309
———. 2001b, Sol. Phys., 203, 233
Yurchyshyn, V. B., Wang, H., Qiu, J., Goode, P. R., & Abramenko, V. I. 2000, ApJ, 540, 1143
Zhang, J., Dere, K. P., Howard, R. A., & Bothmer, V. 2003, ApJ, 582, 520
Zhang, J., & Wang, J. 2001, ApJ, 554, 474